Corrosion Science 232 (2024) 112004

Contents lists available at ScienceDirect

Corrosion Science

journal homepage: www.elsevier.com/locate/corsci

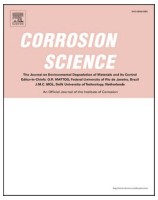

Corrosion mechanisms of plasma welded Nickel aluminium bronze immersed in seawater

Tamsin Dobson [a,*], Nicolas Larrosa [a], Mark Reid [b], Kuladeep Rajamudili [c], Supriyo Ganguly [c], Harry Coules [a]

[a] Solid Mechanics Research Group, University of Bristol, Bristol, UK
[b] Kowari Strain Lab, Australia's Nuclear Science and Technology Organisation (ANSTO), Sydney, Australia
[c] Welding and Additive Manufacturing Centre, University of Cranfield, Cranfield, UK

ARTICLE INFO

Keywords:
Marine corrosion
Nickel aluminium bronze
Biofouling
Corrosion mechanisms
Residual stress
Plasma welding

ABSTRACT

Nickel Aluminium Bronzes (NAB) are copper-based multi-phase alloys used extensively in marine applications. NAB is vulnerable to seawater corrosion, however the interaction between its corrosion mechanisms and real-world factors including biofouling, weld microstructure and residual stress are poorly understood. Seawater corrosion tests were performed on plasma-welded NAB in laboratory and marine environments, demonstrating that the retained β' phase in the Heat Affected Zone (HAZ) experiences Selective Phase Corrosion (SPC), whereas crevice corrosion associated with SPC of the κ_{III} phase occurs at biofouled and stressed areas of parent material. These factors, seldom simulated in physical tests, severely impact NAB's corrosion resistance.

1. Introduction

Nickel Aluminium Bronze (NAB) is extensively used in the marine environment due to its good corrosion resistance and physical properties [1]. It is a multi-phase alloy with a chemical composition that includes a copper content of 76.5 wt% - 85.5 wt% [2], depending on the manufacturing method. Due to this broad categorisation, the chemical compositions can vary significantly between (and even within) samples [3]. NAB manufactured to Defence Standard 02–747 Part 2 [4] contains only the α phase and four intermetallic κ phases as the (undesirable) β and γ_2 phases are heat treated out of the microstructure. κ_I and κ_{II} are Fe-based rosette shaped phases, κ_{III} is a lamellar phase based on NiAl and κ_{IV} is an Fe precipitate found within the α phase [1].

NAB is vulnerable to Selective Phase Corrosion (SPC) when immersed in natural seawater [2,5] especially underneath biofouling and corrosion product deposits. NAB components used on British military vessels are usually manufactured in accordance with one or more of the Defence Standards including Defence Standard 02–747, Defence Standard 02–833 and Defence Standard 02–872. For NAB components to be revalidated under Defence Standard 02–872 Part 3, areas of SPC are identified and repaired before the component can be re-installed and re-used. The use of NAB components in defence marine vessels is important as it is often used for first level parts (i.e. parts that, if they fail, could cause loss of life or loss of the vessel). As such, the failure of NAB has defence and safety implications.

SPC in NAB is classically reported as the accelerated dissolution of the copper-rich α phase within the α-κ_{III} eutectoid, due to the more negative electrode potential of the α phase compared to the κ_{III} phase [6,7]. As the κ_{III} phase forms continuous networks throughout the material, it creates a large surface area of closely adjacent cathodic and anodic regions. This results in a large area of micro-galvanic cells which cause accelerated corrosion localised at the α-κ_{III} boundaries [5]. Ding et al. [8] showed that, when exposed to seawater, the α phase remained unchanged after 180 minutes whilst the α- κ_{III} eutectoid developed a corrosion pit topography (with a maximum depth of 25 nm) after just 60 minutes of exposure.

In strongly acidic environments (pH $<$ 4.0) the anodic-cathodic phase behaviour of the α- κ_{III} eutectoid reverses, resulting in the κ_{III} phase preferentially dissolving out of the material [9]. Within these acidic environments, the corrosion rates can increase up to ten times with the lamellar κ_{III} phase being the most vulnerable phase for dissolution [10] and the continuous nature of the κ_{III} phase means that the corrosion of this phase can significantly effect local mechanical properties.

Localised corrosion is the most concerning for the marine industry due to its stochastic initiation and higher corrosion rates. When NAB is

* Corresponding author.
E-mail address: Tamsin.dobson@bristol.ac.uk (T. Dobson).

https://doi.org/10.1016/j.corsci.2024.112004
Received 29 January 2024; Received in revised form 18 March 2024; Accepted 19 March 2024
Available online 23 March 2024

immersed in corrosive media (such as seawater), localised corrosion occurs when the passivation layer breaks down, allowing accelerated corrosion at discrete sites [11]. Studies into the effect of pitting corrosion often report the deepest corrosion pits in any sample, as these are assumed to be potential failure points in terms of pit-to-crack transition and subsequent fracture (e.g. [1,6,12]). This is also in line with the guidance within API 759–1/ASME FFS-1 [13].

Welding can affect corrosion rates through galvanic corrosion between the weld and parent material, by altering the microstructure in the HAZ (including causing the retention of the martensitic β' phase) and by introducing residual stresses that can enable stress corrosion cracking [14]. Plasma welding was identified as a welding technique that minimized the extent of the HAZ in NAB and was therefore implemented for this study. The heating and cooling involved in welding is affected by phase transformations and has a decreasing effect with distance from the weld pool [5,15–17].

Tensile Residual Stress (RS) created during welding can cause stress corrosion cracking and thus affect the corrosion resistance [14]. Stress assisted pitting corrosion and stress corrosion cracks, caused by RS can act as precursors to failure [18]. Due to this, accurate RS measurements and predictions are crucial for predicting corrosion on welded complex metals, such as NAB.

Many studies have shown that copper alloys are susceptible to Microbially Induced Corrosion (MIC) [8,6,15,16]. This is especially true for metals immersed in natural seawater where biofilms form on the seawater/metal interface [19]. Sulphate Reducing Bacteria (SRB), in particular, are known to increase the rate and severity of corrosion [19, 20] and (along with other bacterial species) encourage the attachment of larger organisms [21–24]

This study uses results from corrosion immersion experiments of welded NAB undertaken in natural seawater (Millbay Marina, Plymouth, UK), simulated seawater and air. The aim is to consider the combined effects of welding and biofouling on corrosion. To do this, the paper investigates the effects of HAZ microstructure on corrosion, the effects of welding induced residual stress (RS) on corrosion and determines the corrosion mechanisms in biofouled areas of NAB. The affects of post welding heat treatment (PWHT) are not included in this study to replicate weld repairs carried out in situ (i.e. at sea) or in haste. As such, the results show the worst case scenario for welds that did not have any PWHT and were not corrosion protected.

2. Methods

Plasma welded NAB coupons were immersed for 12 or 18 months in one of three environments: natural seawater, simulated sea water (SSW) or laboratory air (control). Residual Stress (RS) from the welding process was mapped using neutron diffraction and the HAZ microstructure was characterised. The corrosion mechanisms were evaluated at the end of the immersion periods using SEM, EDX and optical microscopy. Corrosion mechanisms and corrosion rates were compared between each immersion environment and immersion period to evaluate the effect of HAZ microstructure, RS, seawater exposure and biofouling on NAB corrosion mechanisms.

2.1. Immersion tests

As described in [25], cast NAB coupons (Al-9.14, Fe-4.38, Ni-4.84, Mn-0.09, Cu-balance wt%, $\sigma_{0.2}$ = 265 MPa, from the batch testing certificate) were manufactured to a diameter of 200 mm and thickness of 30 mm and then polished toRa = 3.2.

Single-pass bead-on-plate plasma welding was carried out at Cranfield University using 250°C preheating and front wire feeding with plasma torch shielding and trailing shielding (using 100% argon gas). The wire used was 1.2 mm diameter SIFMIG 44 from SIG Consumables (Cu6328 EN 14640). This wire is a popular grade in the marine industry as it is recommended for the welding of cast aluminium bronze alloys exposed to salt [26].

Natural seawater immersion tests were completed at Millbay Marina (Plymouth, U.K.) for 12 months (n=6) and 18 months (n=6), where n is the number of coupons. To replicate the underside of a marine vessel, coupons were suspended 1 m below the seawater surface, with welded surface facing downwards.

The SSW immersion tests and air exposure tests were also carried out for 12 months (n=2 (SSW), n=2 (air)) and 18 months (n=2 (SSW), n=1 (air)). The simulated seawater was mixed in accordance with ASTM D1141–98 [27]. Salinity was maintained close to the maximum of Millbay Marina, pH was maintained to match the pH of the Marina and temperature was maintained close to the warmest global sea temperature. This was done to simulate the worse case corrosion scenario (as per ASTM D1141–98 [27]).

The height of the weld bead was measured on coupons prior to immersion and on natural seawater and air cases post immersion (n=24 for each environment and time period case). Further information on the immersion tests (in natural seawater, simulated seawater and air tests) can be found in Supplementary Data S.1. Physical data for the three environments were taken periodically as presented in [25] and summarised in Supplementary Data S.1.

2.2. Sulphate reducing bacteria (SRB)

An additional coupon was placed in Millbay Marina between January and March 2023 and used to test for the presence of Sulphate Reducing Bacteria (SRB). This additional coupon was also used to evaluate corrosion and biofouling after a 2-month immersion period. After the 2-month immersion period, swabs were taken on the weld (n=4), weld toe (n=4), parent material (n=4), in the seawater close to the coupon (n=3) and in the air above the immersion site (n=3, control samples). Immediately after sampling, the swabs were placed into an iron sulphite agar (Sig Tests®, ECHA Microbiology Ltd.) and incubated at 35°C for 5 days. SRB presence was confirmed by blackening around the swab [28].

2.3. Coupon cleaning and microscopy

After immersion, the 2-, 12- and 18- month immersion period coupons were removed from their test environment and cleaned as per ASTM G1 [29]. This allowed the extent of corrosion underneath the corrosion products and biofouling layer to be observed.

After cleaning, metallography samples were cut from the centre of the weld and parent material using wire electrical discharge machining (EDM). Micrograph samples were taken from coupons prior to immersion (i.e. non-corroded control samples). Four cross-weld samples (length = 200 mm, width = 7.6 mm and depth = 8 mm) were cut from each coupon from standardised positions relative to the weld bead.

Optical microscopy, Scanning Electron Microscopy (SEM) and Energy Dispersive X-Ray Spectroscopy (EDX) were used to image the micrograph samples. A Zeiss Brightfield Microscope was used to image micrographs etched with aqueous solutions of $FeCl_3$ and HCl and unetched micrographs were imaged using a Hitachi TM2020Plus Tabletop Microscope (SEM only) and FEI Quanta 200 FEG-SEM (SEM and EDX). Focus-variation microscopy (Alicona Infinite Focus Microscope) was used to measure corrosion pit depth and width, and weld bead geometry. The Aspect Ratio (AR (ρ), ratio of pit depth (d) to width) was calculated in two different ways, first (as classically used in literature, [30–33]) when the pit width was measured at the pit mouth (w_m) and, secondly, just above the deepest part of the pit (w_d) (Eqs. 1 and 2,. The parameter ρ_d was used to show the "sharpness" of the pit at the deepest point

$$\rho = \frac{w_m}{d} \quad (1)$$

$$\rho_d = \frac{w_d}{d} \quad (2)$$

The corrosion extent measured perpendicularly from the centre of the weld was measured on the cross-weld samples using a ruler. Fig. 1)

2.4. Residual stress measurements

Neutron diffraction using the Kowari Strain Scanner (Australian Centre for Neutron Scattering, ANSTO) was performed to produce a strain map through a cross section of the weld. The strain map used to estimate plasma welding induced Residual Stress (RS) via Hooke's law, however the RS mapped coupon was not subsequently used in immersion tests.

Using neutron diffraction to measure polycrystal deformation and thus calculate lattice strain requires the consideration of elastic anisotropy which describes how crystal stiffness alters depending on the loading direction. This is dependant on the crystal plane (or orientation) described using Miller indices, hkl. Due to this, the Youngs Modulus (E) and Poisson's Ratio (ν), were replaced with plane specific factors E_{hkl} and ν_{hkl} to accurately calculate stress from strain.

As the α phase of NAB is predominantly Cu, a Cu grain orientation was chosen for neutron diffraction sampling. The Cu {311} reflection has been shown to produce the best representation of the bulk material [34] and to have a linear lattice strain response against stress (even into the plastic regime) [35]. As such, the angular dispersive neutron diffraction measurements used the Cu {311} peak.

Measurements of unstrained lattice spacing (d_0) were taken from a comb-type d_0 specimen using a 3×3x3 mm gauge volume. The software QKOWARI was used to carry out Gaussian peak fitting and find the lattice spacing (approx. 1.55 Å). The strain was then calculated in the welded sample using the difference in lattice spacing. E_{hkl} and ν_{hkl} for the Cu {311} plane were calculated using DECcalc software, based on the Kröner polycrystal elasticity model (giving E_{311} = 119.6 GPa and ν_{311} = 0.334). Using these assumptions, Hooke's law was used to calculate stress from the strain outputs in the welded sample.

Uncertainty was calculated using an error propagation method [36]. This involves using the error due to the uncertainty in the peak position (which is dependent on the measurement counting time) and propagating this through to the consequent uncertainty in the stress calculation. Other sources of experimental uncertainty exist such as the assumptions used in the Kröner model, uncertainty in spatial positioning, and any uncertainty in representativeness of the d_0 sample. Therefore, the uncertainties presented represent a lower bound on real uncertainty.

3. Results

3.1. NAB Microstructure prior to immersion

EDX analysis of the parent material (Fig. 2) shows the α phase and the four interstitial κ phases and also confirms the chemical composition as 9.89% Al, 3.75% Fe, 4.71% Ni and 81.66% Cu, wt%. The observed as-cast microstructure is supported by the results of previous publications e.g. [6,10,12,37].

Optical images of the welded samples show the microstructure of the weld material, HAZ and parent material, Fig. 3. The weld material was made up of two phases, the α phase and the (darker) martensitic β' phase, as identified by Li et al. [5]. The HAZ created by the plasma welding method was measured to have a width of 0.96 mm (n = 12, SD = 0.09 mm). It contained a combination of the weld and parent microstructure, with the α phase, martensitic β' phase and the four interstitial metallic κ phases (Fig. 3). Closer to the weld (within the HAZ) there was visibly more β' phase compared to the κ_{III} phase, however a larger proportion of the κ_{III} phase was found with increasing distance from the weld. Outside of the HAZ, no β' phase was found.

3.2. Environmental physiochemical properties and biofouling community

Over the 18 month study in Millbay Marina, seasonal changes in natural seawater temperature, salinity and chlorophyll levels were observed. Maximum seawater temperature and chlorophyll levels were measured in late spring/early summer. The monthly averages (± SD) for salinity, temperature and pH in Millbay Marina and in the simulated environment are shown in Table 1. For the air exposed coupons, air temperature remained in the range 16–23°C.

Sea squirts (Ascidians), Bryozoans (erect and encrusting), and Hydroids, were the main macrofouling organisms observed to settle on the coupons immersed in Millbay Marina (Figure S.3).

3.3. Overall corrosion

Coupons immersed in natural seawater for 12 or 18 months

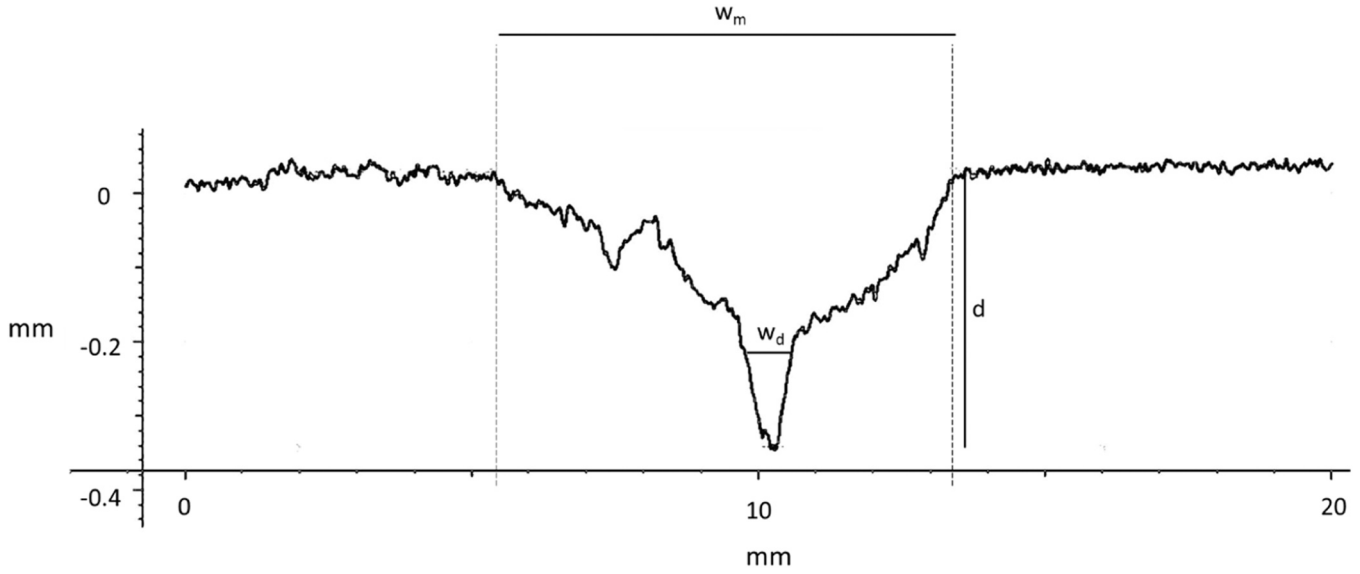

Fig. 1. Corrosion pit cross-section measured using focus-variation microscopy, showing width (at mouth and just above deepest point) and depth measurements as used to calculated Aspect Ratio (AR), ρ and ρ_d.

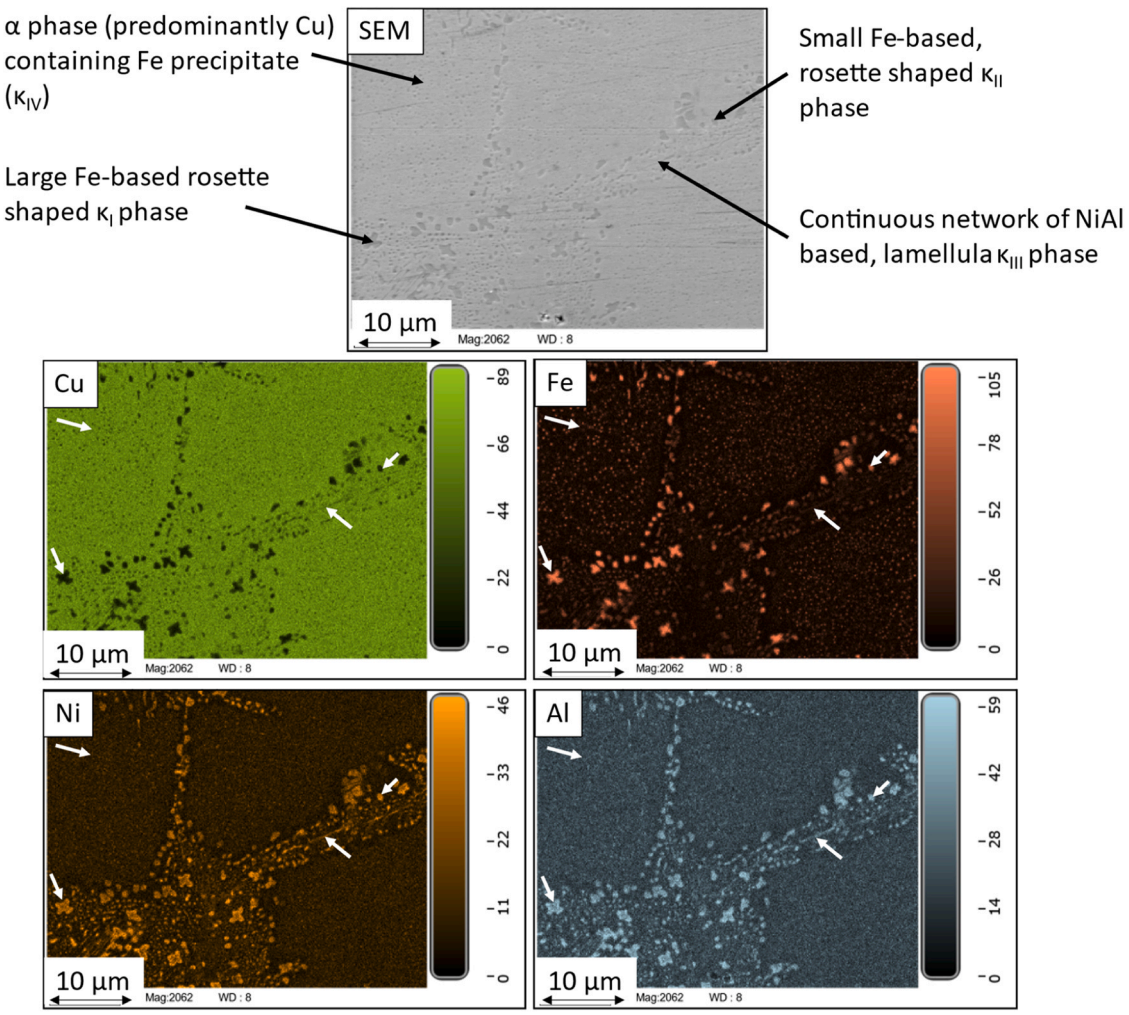

Fig. 2. SEM and EDX images showing a typical as-cast microstructure of Nickel Aluminium Bronze (NAB), showing the constituent phases. Phases were identified in the SEM image by morphology and EDX analysis shows relative amounts of: Cu, Fe, Ni and Al, supporting phase identification (white arrows correspond to the phases identified by the black arrows in the SEM image).

experienced both general and localised corrosion. Localised corrosion mechanisms included erosion corrosion (tribocorrosion) caused by the rope attachment, crevice corrosion, pitting corrosion and corrosion of the weld material (Fig. 4 and Fig. 5).

The 18-month results for the natural seawater immersed coupons show more severe localised corrosion, particularly in areas where macrofouling and corrosion product deposits were found (e.g. Fig. 6). In comparison, very little surface corrosion was seen on the coupons immersed in SSW or air (control), Fig. 7.

3.4. *Weld material corrosion*

The natural seawater immersed coupons experienced significant general and localised corrosion of the weld material (e.g. Fig. 4b, Fig. 5 and Fig. 6). However, SSW immersed coupons experienced only minor general and localised weld material corrosion. In SSW immersed coupons, weld material corrosion was characterised by Cu dissolution (Fig. 8). Air exposed coupons showed sparse general corrosion of the weld material after 12 months with the addition of very minor localised Cu dissolution after 18 months. For coupons immersed in natural seawater, the weld height reduced by 4% after 12 months and 8% after 18 months compared to no significant change in the weld height seen in the SWW immersed or air exposed coupons (12 or 18 months).

Fig. 9 shows example EDX images of weld material after 12 months of immersion in natural seawater. The location of the β' phase correlates with the pattern of oxygen in the EDX images. This illustrates the oxidation of the β' phase in the weld material.

3.5. *Weld toe corrosion and residual stress*

No localised weld toe corrosion was observed in the SSW immersed or air exposed samples after 12 months. However, for the 18-month immersed SSW and air cases, microscopic amounts of localised corrosion were observed at the weld toes. The deepest corrosion pits at the weld toe were measured to be 12 µm and 3 µm (SSW and air coupons respectively). The maximum corrosion pit depth found at the weld toe after 12- and 18- month immersion in natural seawater was 668 µm and 738 µm, respectively (n=24 for each immersion time).

Weld toe corrosion was present in all coupons that had been immersed in natural seawater (2, 12 and 18 month immersion periods). Maximum depths of weld toe corrosion had a linear correlation with immersion period. The mean extent of weld toe corrosion for the 12- and 18- month immersion periods combines (n=96) was 5.5 mm from the centre of the weld (with 12 month immersed mean = 5.8 mm, 18 month mean = 5.10 mm). As the average weld bead measured 3.76 mm from the centre of the weld (mean weld bead width = 7.51 mm), weld toe corrosion extended beyond the HAZ and into the RS effected zone.

The residual stress (RS) was predominantly longitudinal with the highest stress found immediately under the weld bead (sampled at 3 mm depth). As the measured RS was approximately symmetrical around the

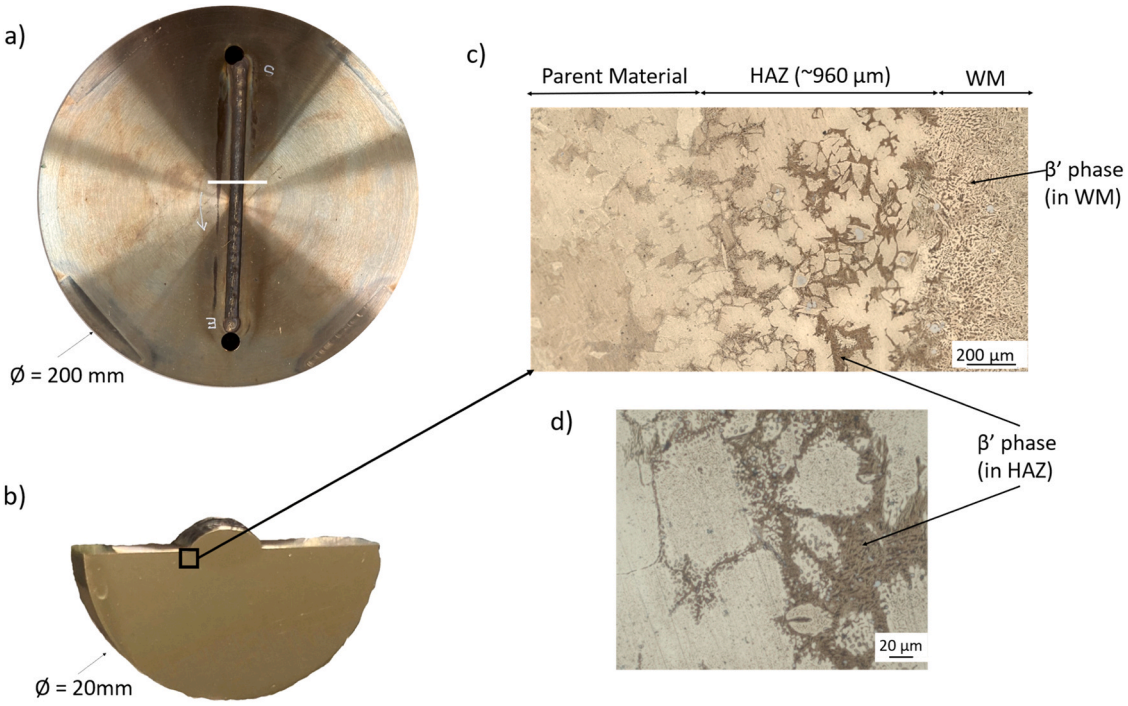

Fig. 3. a) Uncorroded, plasma welded NAB coupon showing metallography sample cross section position. b) Metallography sample from weld cross-section. c) and d) Optical microscope images of the $FeCl_3$-etched uncorroded welded NAB metallography sample. c) The parent material, HAZ and weld material. d) A more detailed optical image from the HAZ showing the martensitic microstructure of the retained β' phase in areas where the κ_{III} phase would be expected.

Table 1
Salinity, temperature and pH of the natural seawater (Millbay Marina) and the simulated environment (SSW tank) averaged from the monthly data.

	Millbay Marina	SSW Tank
Salinity (psu)	31.0	35.4
(± SD)	(± 2.3)	(± 0.5)
(maximum)	*(max = 35.3)*	
Temperature (°C)	13.3	30.4
(± SD)	(± 3.1)	(± 1.5)
pH	7.9	8.3
(± SD)	(± 0.2)	(± 0.1)

weld centre (Fig. 10) the RS measured on the two sides of the weld were taken as n=2 for the longitudinal and transverse stress measured from the centre of the weld outwards. Fig. 11 shows the longitudinal and transverse RS plotted on top of a bar plot that illustrates the extent of surface corrosion out from the weld centre. This suggests a similarity between areas of high residual stress and weld toe corrosion.

SEM images of the weld toe after immersion in natural seawater (Fig. 12) show the corrosion of the β' phase within the HAZ closest to the weld material transitioning to the dissolution of the κ_{III} phase along a gradient moving away from the weld material. This is further evidenced by the EDX output in Fig. 13 showing predominantly Cu dissolution in the HAZ, transitioning to predominantly Al dissolution moving away from the weld into the RS affected parent material. The maximum depth of Selective Phase Corrosion (SPC) along the path of the β' or κ_{III} phase extended well beyond the depth of the corrosion pit at the weld toe, Fig. 13. The maximum depth of κ_{III} phase corrosion seen after 12 months was 1331 µm (from n=19).

3.6. Corrosion mechanisms observed on biofouled areas of the parent material

Seawater swabs taken from the middle site in Millbay Marina reacted positively to the sulphate reducing bacteria (SRB) assay test proving that SRB were present in the seawater and on all sampled areas of the coupon.

After immersion in natural seawater, maximum pit depths were sampled on biofouled areas of the parent material, Fig. 14. No significant difference was found in the mean or maximum pit depth on samples immersed for 12- or 18- months. However, the corrosion pit diameters in 18- month immersed samples were 17% larger than in 12-month immersed samples. The brighter areas of green within the corroded areas imaged by EDX (e.g. Fig. 14b) show higher density Cu regions. Previous studies [6,37] have suggested that Cu redeposition occurs in the areas vacated by the dissolution of the κ_{III} phase, which could explain the higher density of Cu in these regions.

The deepest corrosion pit measured on a biofouled area of the parent material was 986 µm (mean = 241 µm, SD = 210 µm, n = 155). SEM images evidenced κ_{III} phase SPC extending well beyond the bottom of the measured corrosion pits (as observed in corrosion pits at the weld toe). The mean Aspect Ratio (AR) for corrosion pits found in biofouled areas was 0.08 (n=155, SD = 0.05). This compares to the weld toe corrosion pits that had a mean AR of 0.12 (n=65, SD=0.08), Fig. 15.

A sample of 10 pits found in biofouled areas of the parent material of coupons immersed in natural seawater for 12 months were assessed for morphology. 50% could be described as large shallow or ellipsoidal pits and 50% were cone shaped or nipple shaped. These categories were easily separated by comparing the average Aspect Ratio (AR, ratio of pit depth (d) to width) of the pits at the deepest part of the pit (ρ_d). Whilst the mean overall AR (ρ) for cone and nipple pits was 0.11 and the mean overall AR for large shallow and ellipsoidal pits was 0.18, the mean ρ_d for the cone and nipple shaped pits was 2.48 whilst the mean ρ_d for the for large shallow and ellipsoidal pits was 0.63 (Fig. 16). This indicator for corrosion pit morphology is used to show the "sharpness" of the pit at its deepest point.

3.7. Corrosion products

Chemical analysis of the corrosion products from coupons immersed

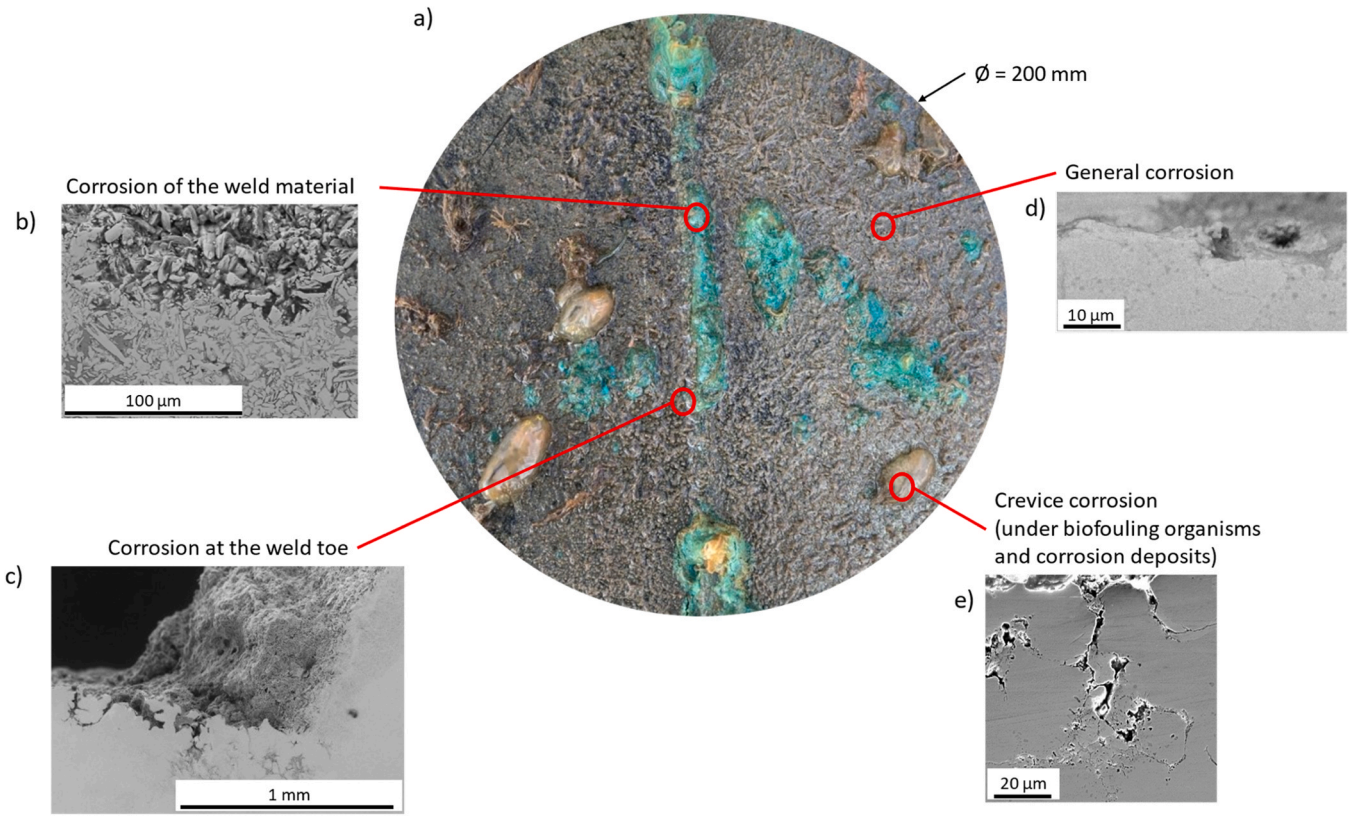

Fig. 4. a) Pre-cleaning photograph of a natural seawater immersed coupon removed from Millbay Marina after 12 months. The surrounding SEM images (taken post cleaning, cutting and polishing) show the different corrosion mechanisms seen in b) the weld material, c) at the weld toe, d) general corrosion of the parent material and d) crevice corrosion (with selective phase corrosion) found underneath biofouling organisms and corrosion product deposits.

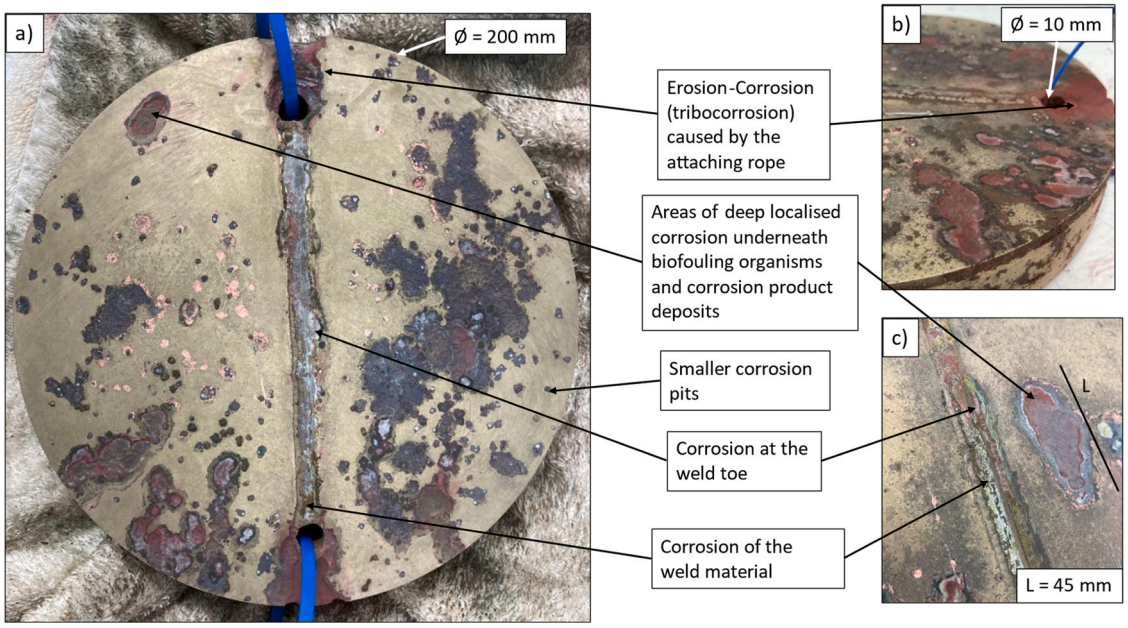

Fig. 5. Post-cleaning photographs of 3 natural seawater immersed coupons removed from Millbay Marina after 12 months. a) Whole coupon showing a variety of corrosion types, b) side view showing erosion corrosion (tribocorrosion) from the attaching rope and c) corrosion on the weld, at the weld toe and localised on an area of the parent material.

in natural seawater showed the presence of sulphur (mean weight percentage (wt%) ± standard deviation (SD) 2.3% ± 1.1%, mean wt% ± SD, n=4). Fig. 17 shows that the green corrosion products were high wt % copper and oxygen, the white corrosion products were high wt% aluminium and oxygen and the brown/orange corrosion products were high wt% iron and oxygen. Corrosion product on the parent metal showed aluminium as the highest wt% whilst the corrosion product sampled from the weld material showed copper as the highest wt%.

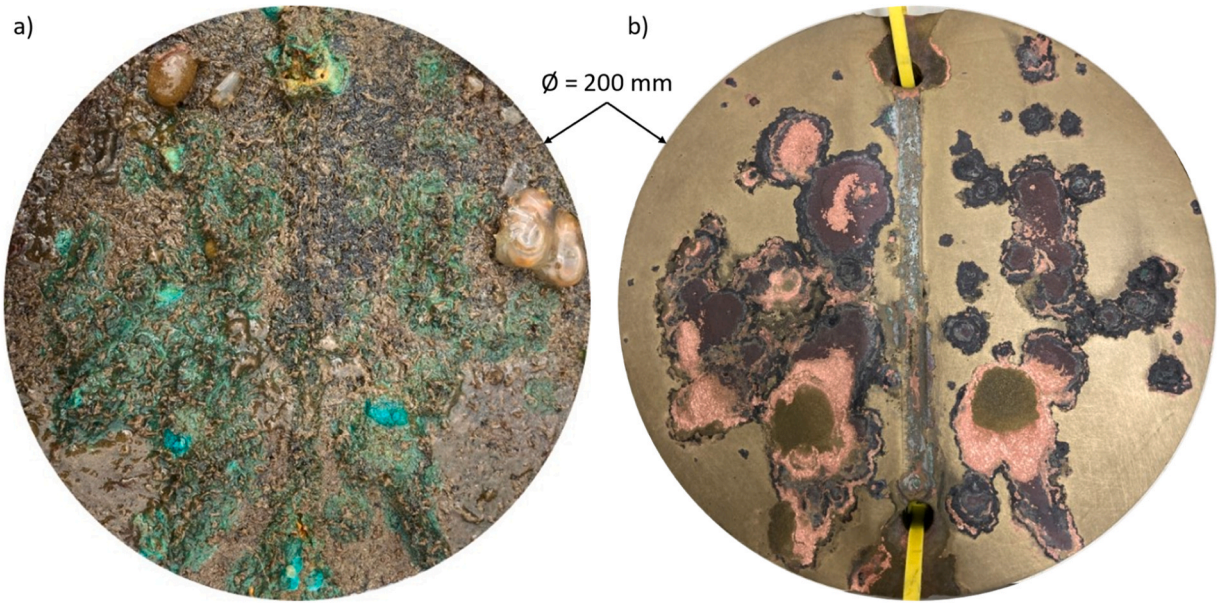

Fig. 6. a) Coupon immediately on removal from natural seawater after an 18-month immersion period. b) The same coupon, after cleaning.

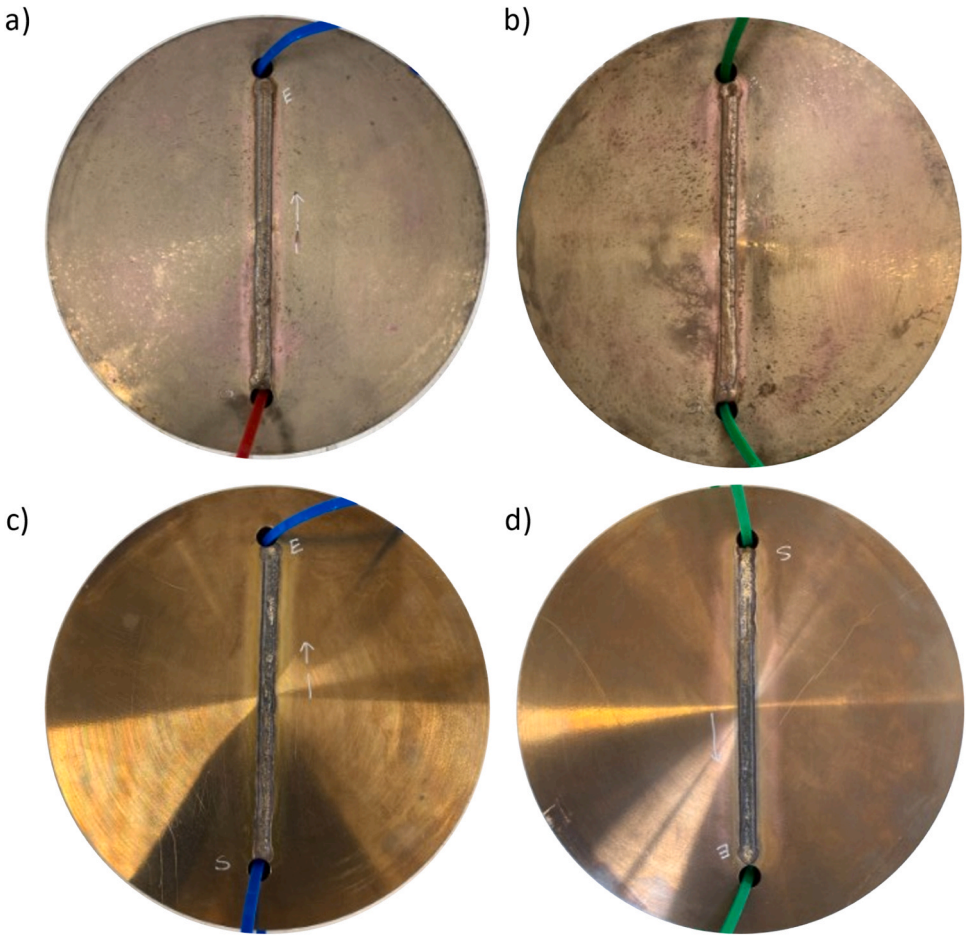

Fig. 7. a) 12-month SSW immersed coupon b) 18-month SSW immersed coupon c) 12-month air exposed coupon and d) 18-month air exposed coupon. All images are post-cleaning.

Chemical analysis of the corrosion products from coupons immersed in simulated seawater also showed the presence of sulphur (3.2% ± 2.0%, n=6). Corrosion products from SSW immersed coupons were found inside the drill holes of the coupons (seen in Fig. 5) and on the underside of the coupons where the contact between the coupon underside and rubber matting on the SSW tank bottom created a crevice

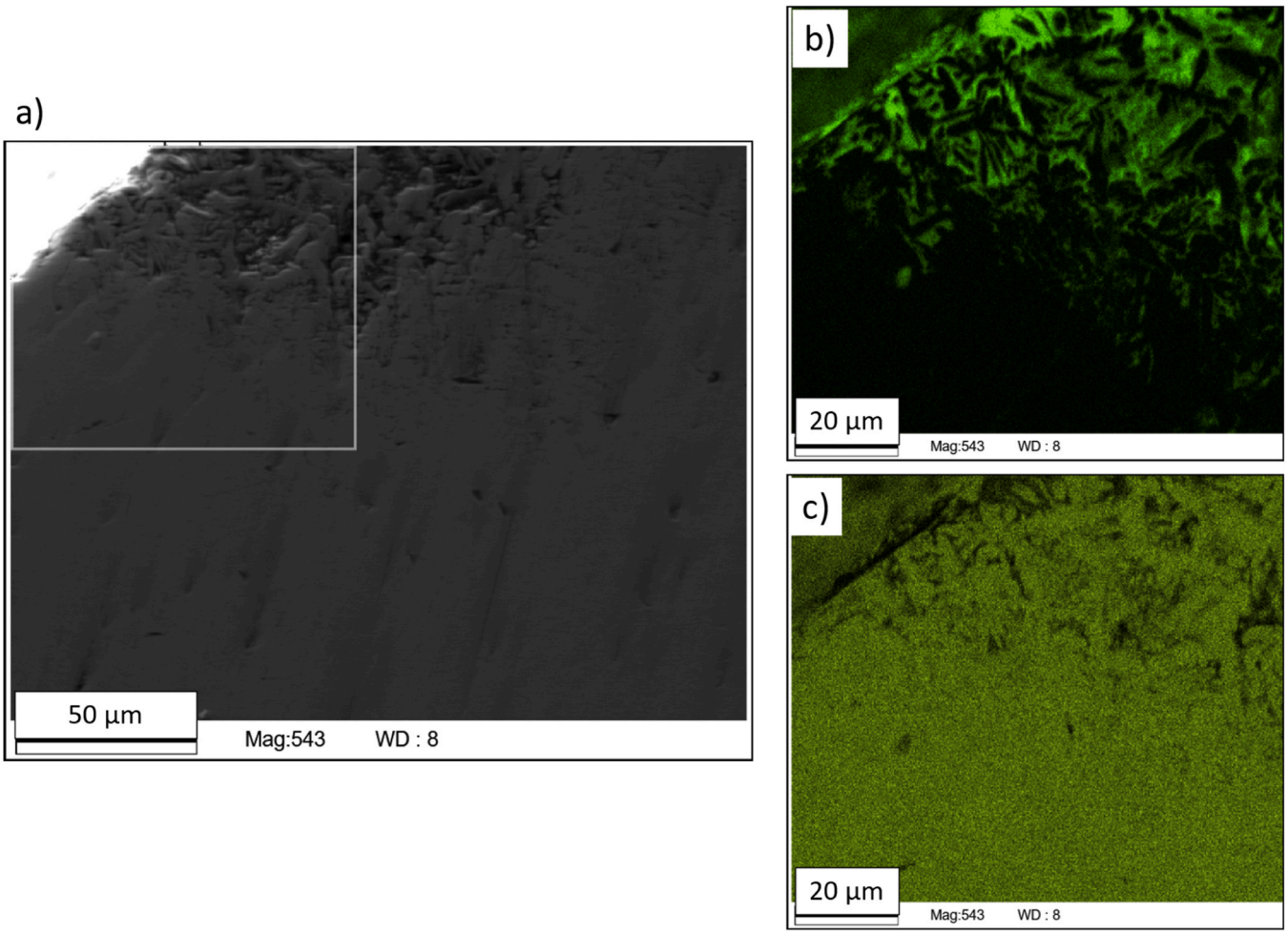

Fig. 8. a) SEM image of an 18-month SSW immersed sample showing the EDX position relative to the edge of the weld bead. b) EDX output showing oxygen content and c) EDX output showing Cu dissolution in the weld material.

corrosion environment.

4. Discussion

Significant differences in corrosion mechanism were seen between the different immersion environments. Air exposure of polished, plasma welded NAB coupons caused no significant localised corrosion and only low levels of weld toe corrosion (characterised by copper dissolution) after 18 months exposure time. SSW immersion for 18 months caused the corrosion of the weld material, characterised by Cu dissolution. Natural seawater immersion however caused severe localised corrosion in the HAZ, Residual Stress (RS) affected area and underneath biofouling organisms and corrosion product deposits.

Localised corrosion occurs when the passivation layer breaks down [37–39]. There is greater opportunity for this to occur in natural seawater compared to the simulated (tank) environment due to the effect of microfouling, macrofouling, high water velocity and/or turbidity. This could begin to explain the difference in localised corrosion seen in natural seawater vs simulated seawater immersion coupons.

The corrosion product analysis (Fig. 17) supports the findings of Wharton and Stokes [37] who used EDX to show that the corrosion products of NAB samples in natural seawater were formed of three layers (a green cap, middle brown layer and white layer on the metal). They suggested that the green (outer) layer was predominantly $Cu_2(OH)_3Cl$, the brown (middle) layer predominantly Cu_2O and the white (inner) layer CuCl. However, Fig. 17 also suggests the presence of aluminium oxide in the inner white layer, which could be caused by the preferential dealuminification of the κ_{III} phase. This is supported by the results of Lv et al. [40] who showed that, in the presence of pH < 3.5, the κ_{III} phase was preferentially corroded due to its lower Volta potential, producing Al_2O_3 and $Al(OH)_3$ (along with copper oxides and chlorides) in the corrosion products.

In addition, previous studies have shown that aluminium oxides are key in the formation of the protective layer on the surface of NAB [41, 42] and some researchers have shown that it is composed of a dense inner layer of Al_2O_3 and a porous outer layer of Cu_2O [43–45]. Ding et al. [8] observed the formation of the protective film using in-situ atomic force microscopy. Their results show that the corrosion resistance of the κ_{III} phase can be explained by its ability to form a stable and dense protective film within a short time, whilst the β' phase is less able to form the protective film and therefore suffers the most severe corrosion.

For welding process development, the significant reduction in weld bead height seen in natural seawater immersed samples (4% annual height reduction) highlights the need to refine welding techniques to reduce the vulnerability of weld material to corrosion (particularly SPC of the β' phase) when immersed in natural seawater. This will be particularly important for the development of improved additive manufacturing methods for Nickel Aluminium Bronze (NAB) [46–48].

The characterisation of different areas of the welded coupons along with correlation features observed in those areas are summarised in Table 2.

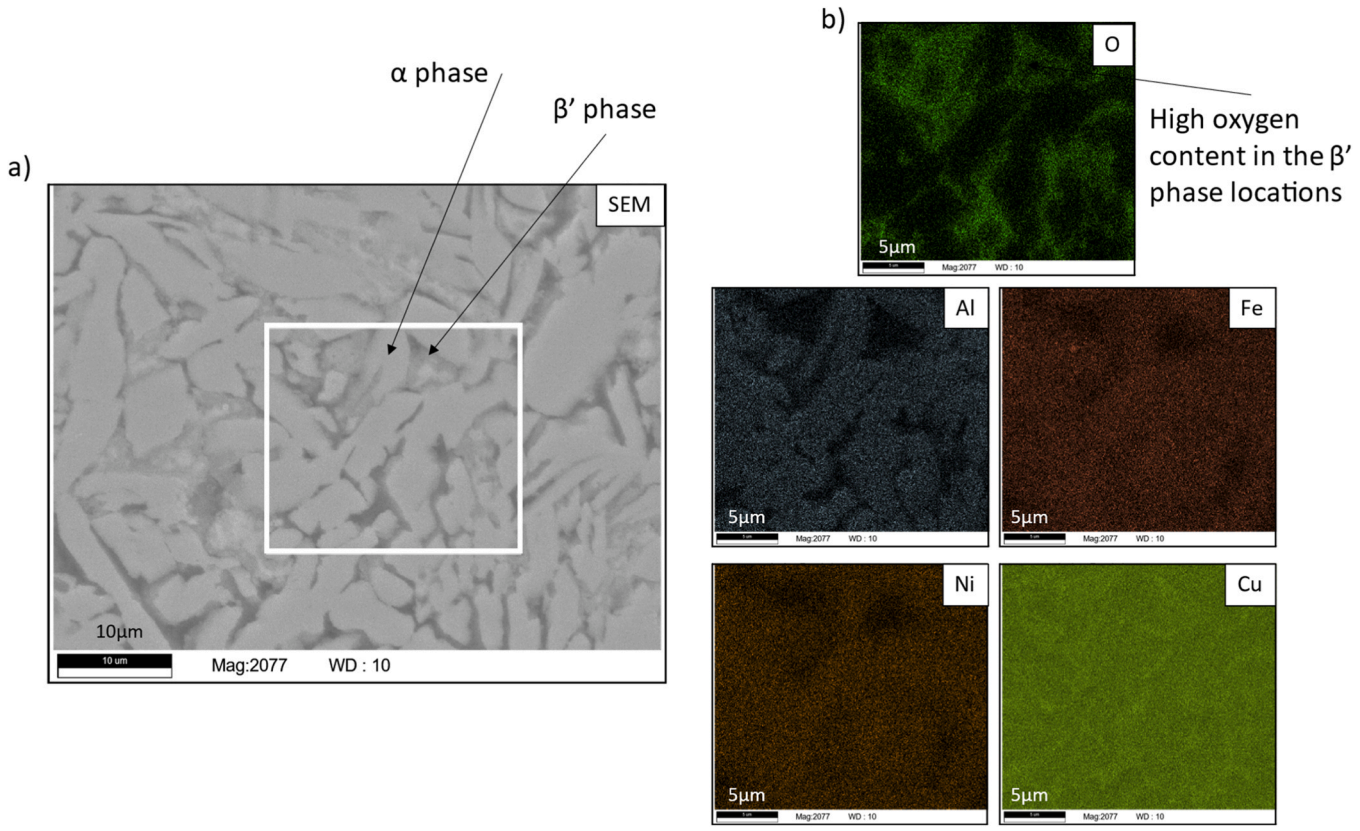

Fig. 9. a) SEM image of the weld material after 12-months natural seawater immersion showing the area of EDX analysis. b) EDX images of the elements: oxygen, aluminium, iron, nickel and copper.

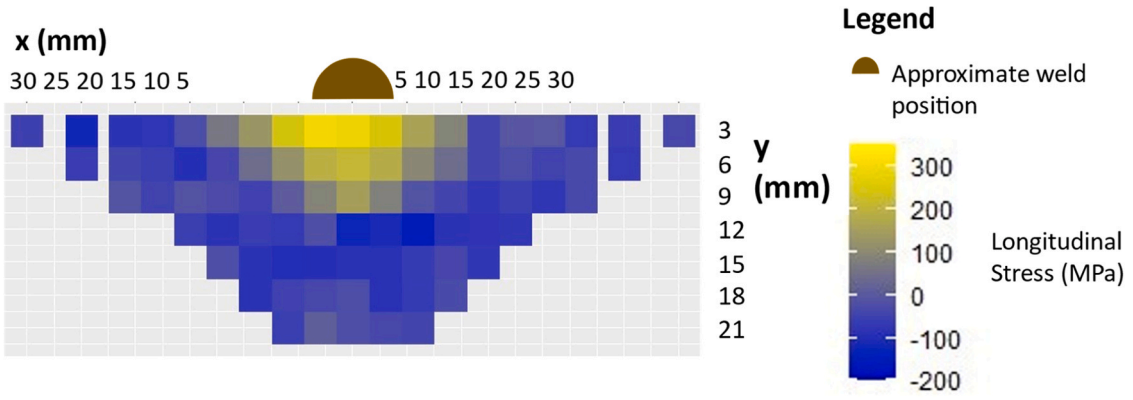

Fig. 10. Neutron diffraction map of longitudinal stress through the cross section below the weld (approximate weld position indicated).

4.1. HAZ microstructure and RS effects on corrosion mechanisms

The HAZ microstructure observed prior to immersion (Fig. 3) shows that the HAZ had an average width of <1 mm. Outside the HAZ, the temperature did not reach above the eutectoid point and therefore the α-κ_{III} eutectoid was retained, however within the HAZ, where the temperature rose above the eutectoid point the β phase was retained. This caused a gradient of β' to α-κ_{III} eutectoid microstructure seen in Fig. 3.

This supports the results of Li et al. [5] who (using a gas metal arc welding process shielded with 100% argon gas) also produced a HAZ width of < 1 mm. Li et al. observed that the martensitic β' phase was retained in areas of the HAZ where the temperature increased above the eutectic point during the welding process.

This gradient is reflected in the SPC within the HAZ of natural seawater immersed samples with SPC of β' phase in the HAZ transitioning to SPC along the κ_{III} phase relating to phase availability. This is evidenced in Fig. 12 and Fig. 13. These results support previous studies that show the β' phase as vulnerable to SPC [8] and that the continuous geometry of the κ_{III} phase causes it to be vulnerable to corrosion [6,37]. The preferential dissolution of the κ_{III} phase at the weld toe is confirmed by the high wt% of Al measured in the corrosion products sampled from that area (Fig. 17).

The heat treatment carried out during material manufacture meant that no β' phase was retained in the parent material (outside of the HAZ). Therefore, the only area where the β' phase and κ_{III} phase both exist was in the HAZ. The results suggest that the change from β' phase to κ_{III} phase SPC within the HAZ corresponded to phase availability (with more κ_{III} phase available further from the weld). However, this could also be due to relative corrosion potentials between the two phases where the volt potential order of the phases has been shown to be κ

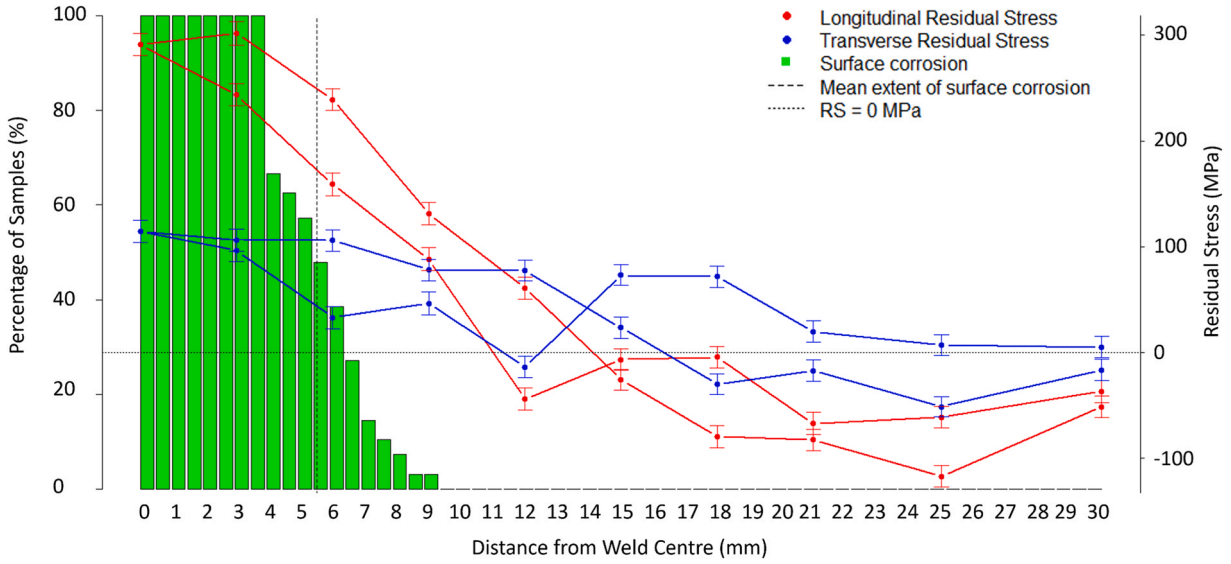

Fig. 11. Green bar plot shows the extent of surface corrosion measured at the weld toe of 12- and 18- month natural seawater immersed coupons (n=96). The mean surface corrosion extent of 5.5 mm is shown. The longitudinal (red, n=2) and transverse (blue, n=2) near-surface residual stress measurements for both sides of the weld on an uncorroded coupon are overlayed for comparison. Error bars on the RS data points show uncertainty estimates ($u_{\sigma x}$ [36]) in neutron diffraction calculated residual stress (MPa).

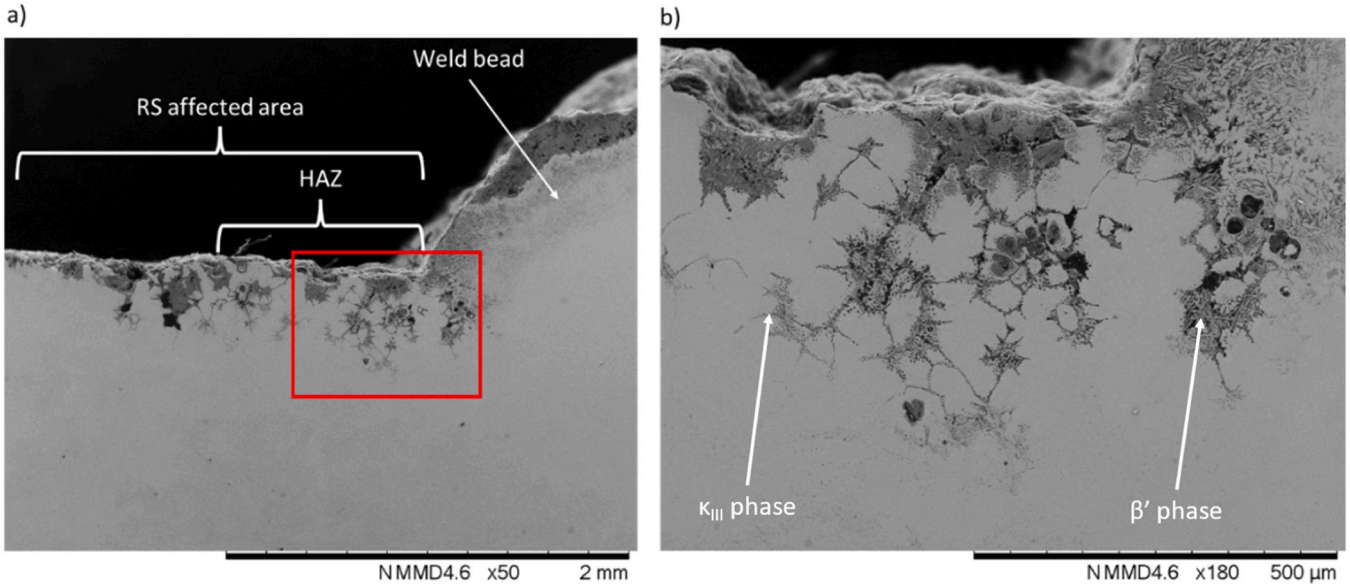

Fig. 12. Large scale SEM images indicating corrosion severity in the RS affected area and HAZ. a) SEM image showing a cross section of a NAB weld toe (with weld bead on the top right of the image) after 18-month immersion in natural seawater. b) SEM image from the red box in a) showing SPC of the β' phase close to the weld material transitioning to SPC of the κ_{III} phase further from the weld material.

phases > β' phase > α phase [40,49].

The average extent of surface corrosion at the weld toe (for the 12 and 18 month immersion periods combines) was 5.5 mm from the centre of the weld. This means that weld toe surface corrosion extended beyond the HAZ and into the RS-affected zone of the parent material. Culpan and Foley [6] suggested that RS accelerates corrosion by opening up corroded areas (allowing more ingress of seawater) and by disrupting the protective oxide film. This could explain the severe corrosion observed outside of the HAZ.

The extent of corrosion from the weld toe appears static after the initial 12-month immersion period. This could be due to sedimentation and biofouling, as found by [12] or due to a reduction in the general corrosion rate, as suggested in [25].

The results suggest that NAB corrosion in SSW is predominantly via the dissolution of Cu, whilst NAB corrosion in natural seawater is predominantly via SPC of the κ_{III} phase (i.e. de-aluminification). This is supported by the SSW immersed coupon corrosion products that had a significantly larger wt% of Cu (22.1% ± 22.9%, mean ± SD) compared to the corrosion products from the coupons immersed in the natural environment (8.8% ± 4.3%), Fig. 17.

From these results, it is recommended that future welding processes developed for NAB focus on reducing residual stresses and the width of the HAZ. This will reduce the SPC of the κ_{III} phase in the residual stress affected areas and reduce the amount of (the corrosion vulnerable) β' phase at the weld toe. The most practical techniques to achieve a reduction in RS would be to use a greater pre-heating temperature or to

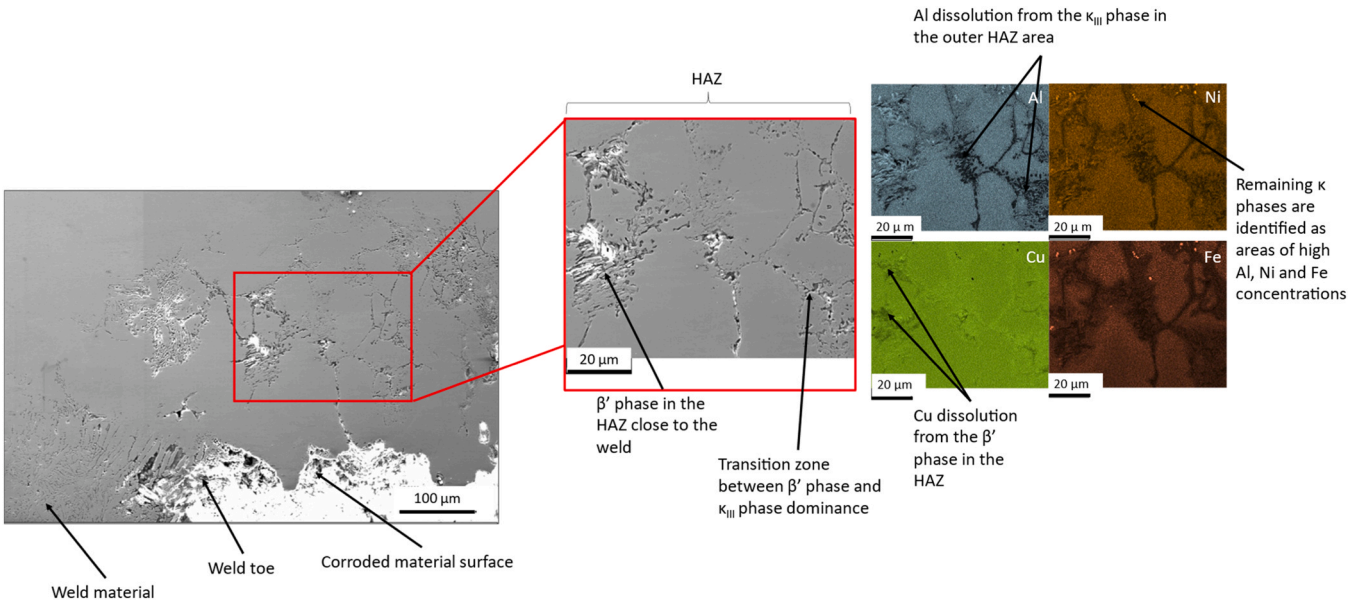

Fig. 13. SEM and EDX images of the HAZ and RS effected area of a 12-month natural seawater immersed sample. Cu dissolution is seen in the HAZ as the predominant corrosion mechanisms whilst Al dissolution is seen as the dominant corrosion mechanisms in the parent material in the RS-affected area.

use post welding heat treatment [50]. However, both of these techniques could alter the microstructure and thus create other undesirable material properties if not applied carefully.

4.2. Sulphate Reducing Bacteria (SRB) effects on corrosion

Sulphide pollution is known to exacerbate corrosion of metals (e.g. [51,52]). Sulphur was found in the corrosion products of natural and simulated seawater immersed coupons. In the natural marine environment sulphur rich areas can be created by algae, bacteria, pollution sources (including storm drain overflow outputs) and seawater salts. X-ray analysis performed by Schüssler and Exner [41] identified copper sulphides in the inner region of corrosion products on NAB samples. They suggested that the incorporation of copper sulphides changed the structure of the passivating layer and thus increased the corrosion rate. In the natural seawater immersed samples of the present study, the largest wt% of sulphur was found in the inner (white) corrosion product.

Characklis [53] stated that corrosion caused by Sulphate Reducing Bacteria (SRB) is characterised by conical pits containing concentric rings. These geometries were visible in some of the SEM images of corrosion pits from the natural seawater immersion tests (Supplementary Figure S.4). All the natural seawater induced corrosion pits showed geometric complexity supporting the conclusions of Gomez de Saravia et al. [54] that copper-nickel alloys create complex corrosion patterns due to local and general corrosion occurring simultaneously alongside microbial induced corrosion. The importance of this on stress concentration is discussed in [55].

It is probable that the sulphur found in the corrosion products of SSW immersed coupons was derived from the sodium sulphate in the simulated seawater (as per ASTM D1141–98 (2021) [27]). However, the amount of sulphur in the simulated environment could have been increased by contamination. This could have been due to sulphur leaching out of the (sulphur-vulcanised) rubber at the bottom of the tank as all of the corrosion products were taken from the underside of the coupon where crevice corrosion had occurred between the coupon underside and the rubber bottom of the tank. However, no evidence of SRB induced corrosion pits was found on the SSW immersed coupons so any sulphur contamination is assumed to have had no significant effect (due to the significantly lower corrosion rate and extent found on the SSW immersed coupons compared to the natural case).

4.3. Corrosion on biofouled areas

The maximum corrosion pit depth measured on a biofouled area of NAB parent was 986 μm. This is deeper than corrosion pits previously reported for artificial crevices on NAB samples [12,37]. Oakley et al. [12] measured the maximum depth of crevice corrosion under artificial crevices as 580 μm (on NAB immersed for 12 months in once-through natural seawater at 7–19 °C) whilst Wharton and Stokes [37] found 400–500 μm deep anodic trenches under artificial crevices after a 12 month natural seawater immersion test.

In addition, Oakley et al. [12] measured κ_{III} phase SPC underneath the crevices that reached 350 μm to 500 μm beyond the depth of the crevice. This suggests that Oakley et al. observed a maximum SPC depth of 1080 μm. The maximum κ_{III} phase SPC measured in the current results, was over 20% deeper than this, 1331 μm. The deeper corrosion and SPC found in biofouled areas in these results compared to underneath artificial crevices could be due to the bio-adhesives used by the organisms [56–58] or due to geometric differences between the artificial crevices used by previous researchers [12,37] and the macrofouling organisms seen in this study.

80% of the corrosion pits included in Fig. 15 showed maximum depth in the centre of the pits with the cone and nipple morphology being the most extreme example of this. As such, the morphology of corrosion pits found in biofouled areas of the parent material was consistent with critical crevice solution theory where the hydrolysis of metal ions within crevices results in the reduction of pH causing corrosion initiation in the centre of the crevice (thus causing maximum depth at the pit centre) [59]. This suggests that the solution underneath macrofouling organisms was acidified, allowing crevice corrosion initiation. This is supported by the results of Zhang et al. [60] who measured acidification of the solution underneath macrofouling organisms on stainless steels.

Neodo et al. [9] and Nakhaie [49] showed that when pH < 4.0, the κ_{III} phase is preferentially dissolved from the α -κ_{III} eutectoid in NAB. Whilst there is no data showing the exact pH underneath the biofouling organisms seen in this study, previous research [61] showed that the effects of barnacle cement on stainless steel 316 L were similar to the effects of an etchant of composition 15 ml HCl, 10 ml, HNO_3 and 10 ml acetic acid. Combining the results from these studies with the results seen in the present study suggests that SPC of the κ_{III} phase occurs underneath macrofouling organisms due to localised solution acidification.

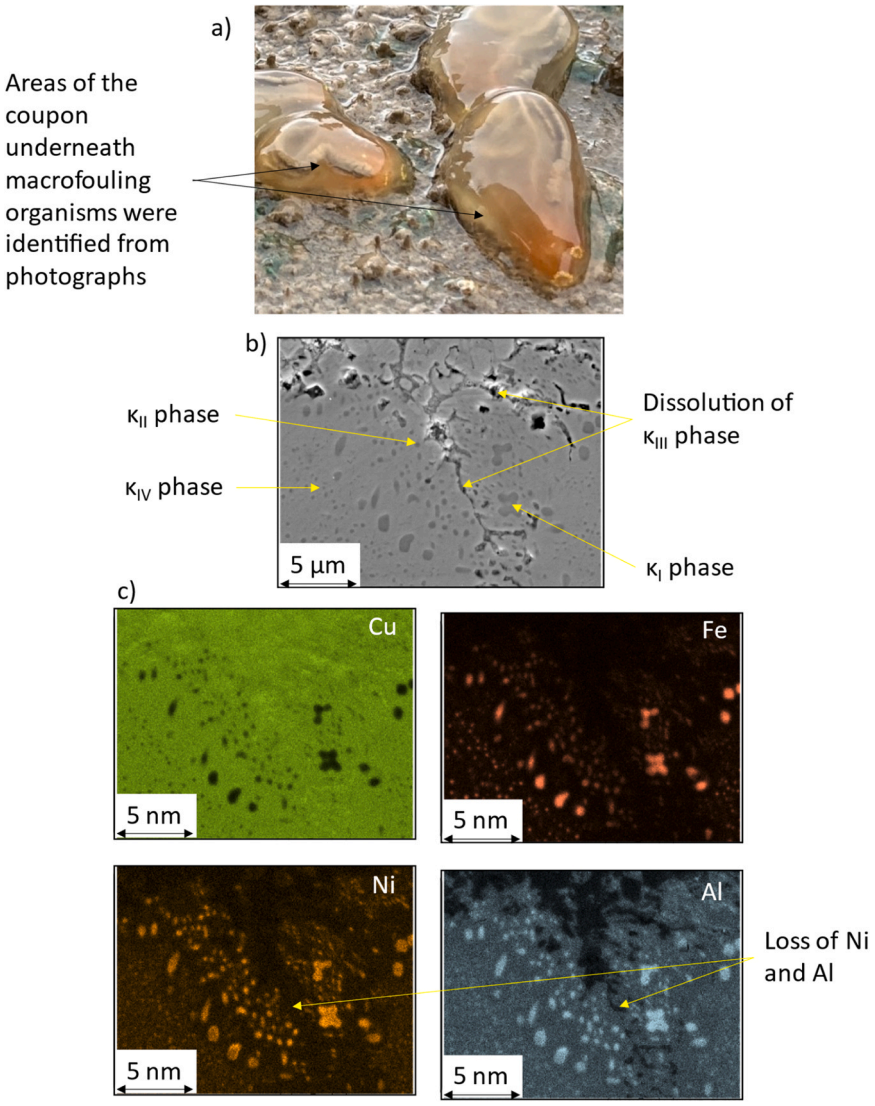

Fig. 14. a) Macrofouling organisms (Ascidians) attached to a coupon surface after natural seawater immersion. b) SEM image of a macrograph taken from a biofouled area of the parent material with the coupon surface towards the top of the image and c) EDX images showing dissolution of the Fe, Ni and Al rich phases (the κ-phases) in the corroded regions with denser Cu regions seen in the vacated areas.

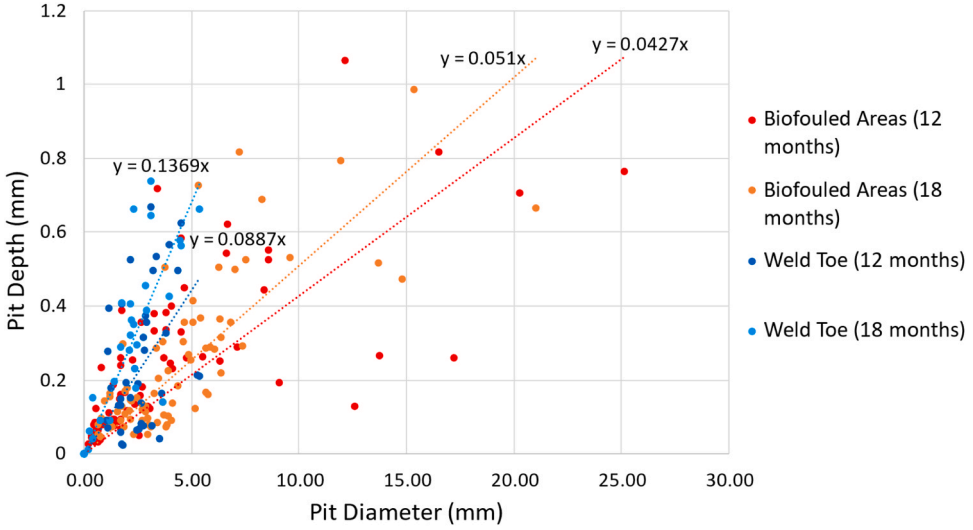

Fig. 15. Aspect Ratio of corrosion pits found in biofouled areas of the parent material and at the weld toe for the 12 and 18 month immersion periods.

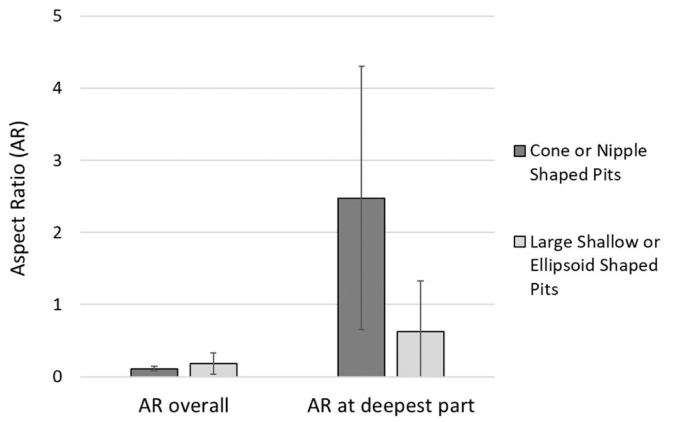

Fig. 16. Aspect ratio (AR) and AR when the width is measured just above the deepest point of the pit (AR_d) for cone or nipple shaped pits vs large shallow or ellipsoidal shaped pits.

Fig. 15 shows the significantly higher aspect ratio of weld toe corrosion pits compared to corrosion pits found on the parent material suggesting that, even without considering the effect of weld induced RS, these would be more likely to be the pit that transitions to a propagating crack and subsequently becomes the fracture initiation point.

4.4. Inspection and revalidation of NAB components immersed in natural seawater

The presented results suggest that inspections of NAB components/structures immersed in natural seawater should focus on areas vulnerable to crevice corrosion or affected by residual stress (i.e. areas under macrofouling organisms or close to welds). The inspections should concentrate on areas that have experienced crevice corrosion as these areas could be experiencing SPC of the κ_{III} phase. In these areas localised corrosion rates could be very high and could cause premature fracture and failure of the component.

This supports the current suggestions in Defence Standard 02–873 Part 3 which is used to revalidate NAB components before their re-use. Revalidation in accordance with this standard focusses on areas of SPC and is used to establish the extent of any SPC, the acceptability of any weld repairs and the final wall thickness. The standard states that SPC of the κ_{III} phase can penetrate NAB walls up to 1.1 mm per year, whilst this study shows that the dissolution of the κ_{III} phase can penetrate up to 1.3 mm per year (a difference of 0.2 mm per year).

Under the rules of SOLAS [62], marine vessels are allowed up to 5 years between dry docks. However, warships are officially except from this requirement, allowing them to go for longer between major dry dockings if military actions require it.

If the 5 year dry docking period stated in SOLAS is taken as an ideal period between major inspections, this could lead to an underestimation

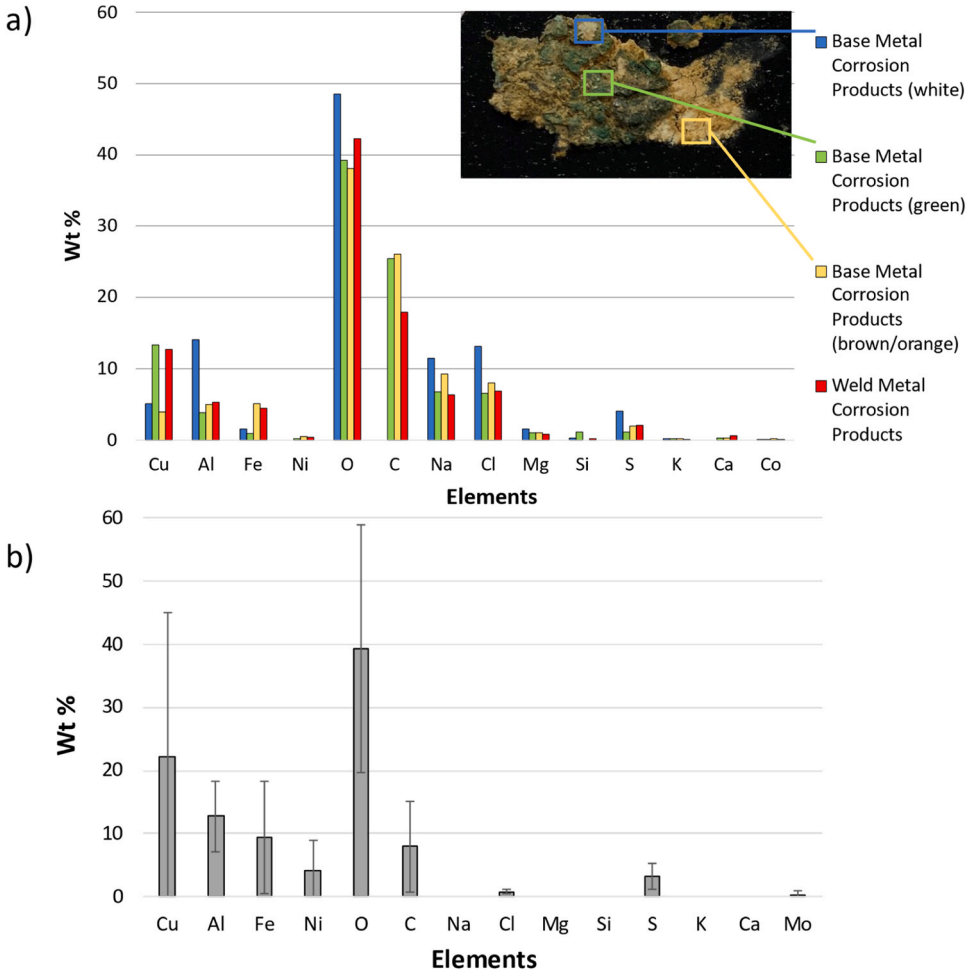

Fig. 17. a) Chemical composition (weight percentage, wt%) of corrosion products found on the parent material and weld material after 18-months immersion in natural seawater. The corrosion products found on the parent material were layered with copper oxide as the outer layer, aluminium oxide as the largest middle layer, and iron oxide as an additional (smaller) inner layer. The weld material corrosion products were more mixed. b) Chemical composition (weight percentage, wt %) of corrosion products found on the parent material after 18-months immersion in simulated seawater (SSW), taken in 6 positions with SD shown.

Table 2
Coupon area characterisation and corrosion features identified.

Coupon Area	Microstructure Characterisation	Corrosion Features Observed in the Area	Figure(s)
Weld material	Predominantly α and β' phases	SPC of the β' phase	Fig. 4b
HAZ	Predominantly α and β' phases transitioning to α and κ phases away from the weld	SPC of the β' phase transitioning to SPC of the κ_{III} phase away from the weld	Fig. 12 and Fig. 13
RS affected area (outside of the weld and HAZ)	α and κ phases	SPC of the κ_{III} phase	Fig. 12 and Fig. 13
Biofouled areas of the parent material	α and κ phases	SPC of the κ_{III} phase observed in biofouled areas	Fig. 4e and Fig. 14
Parent material	α and κ phases	General corrosion (predominantly dissolution of the α phase)	Fig. 4d

of assumed corrosion depth of up to 1 mm (0.2 mm multiplied by 5 years). Typical NAB components (such as the NAB pump described by Hazra and Balan [63]) will have wall thicknesses varying between 5 mm - 50 mm, this could lead to an underestimation of corrosion that is equivalent to 2% - 20% of the wall thickness which could lead to a significant reduction in strength and consequential failure under load. This is particularly relevant when Defence Standard 02–873 Part 3 states that:

"Castings whose thickness has been reduced by more than 10% below the drawing thickness are to be REJECTED."

Most NAB component designs would include additional safety factors such as shock factors (against underwater explosions), human factors (e.g. Defence Standard 00–251, ASTM F1337 – 22 and the ABS Guidance Document [64]) and general engineering judgement. However, it is possible that some designs would be pushed to the limit of the Defence Standard wall thickness requirements due to other design requirements (such as total mass, due to stability requirements, or budget limitations). As such, the Defence Standard 02–873 Part 3 recommendations may need to be reconsidered following the changing physiochemistry of natural seawater and our growing understanding of the effect of biofouling on SPC in NAB.

To support this, a recent review of corrosion and biofouling by Vuong et al. [65] highlighted the need to use holistic, multi-disciplinary approaches to understand biofouling drivers of corrosion and corrosion mechanisms. This paper responds to this industry need as it includes the effects of natural seawater variability (e.g. temperature, salinity, chemical composition) and the effect of biofouling. These effects would not have been considered in an SSW-only study.

5. Conclusions

The β' phase is retained in the HAZ of plasma welded NAB and is preferentially corroded when immersed in natural seawater. This phase could be heat-treated out of the material post welding to prevent this SPC in the HAZ. In the RS affected area (just outside the HAZ), SPC of the κ_{III} phase was observed. Future welding process development should aim to reduce the width of the HAZ and/or prevent the retention of the β' phase in the HAZ of the final material and to include techniques that will reduce welding induced residual stress.

Welding techniques need to be developed to reduce the vulnerability of weld material to corrosion (particularly SPC of the β' phase in NAB). This will be particularly important for the development of improved additive manufacturing methods. As these results highlight RS as a contributing factor in corrosion. Welding process development that reduces RS will therefore benefit corrosion resistance of the welded component.

Biofouled areas of NAB are vulnerable to crevice induced corrosion. Corrosion pits in biofouled areas measured to be >20% deeper than previously reported to be caused by artificial crevices. This means that biofouling prevention and/or early removal could act to reduce the appearance of corrosion pitting in NAB immersed in natural seawater.

There is a clear difference in corrosion severity between NAB immersed in natural seawater and NAB immersed in simulated seawater or exposed to air. This highlights the importance of testing in the natural seawater environment. Defence Standard 02–873 Part 3 (and similar) recommendations may need to be updated to include the effects of current seawater physiology and the effects of biofouling.

CRediT authorship contribution statement

Tamsin Dobson: Writing – review & editing, Writing – original draft, Methodology, Investigation, Funding acquisition, Formal analysis, Data curation, Conceptualization, **Nicolas Larrosa**: Writing – review & editing, Validation, Supervision, **Mark Reid**: Data curation, **Kuladeep Rajamudili**: Data curation, **Supriyo Ganguly**: Supervision, **Harry Coules**: Writing – review & editing, Supervision, Funding acquisition.

Declaration of Competing Interest

The authors declare that they have no known competing financial interests or personal relationships that could have appeared to influence the work reported in this paper.

Data availability

Data will be made available on request.

Acknowledgements

The authors acknowledge the support of ANSTO in providing access to instruments, capabilities and facilities used in this via Proposal 13838. This work was supported by the EPSRC [grant number EP/R513179/1] and Babcock International [studentship number 2019 - 4720].

Appendix A. Supporting information

Supplementary data associated with this article can be found in the online version at doi:10.1016/j.corsci.2024.112004.

References

[1] J.A. Wharton, R.C. Barik, G. Kear, R.J.K. Wood, K.R. Stokes, F.C. Walsh, The corrosion of nickel-aluminium bronze in seawater, Corros. Sci. 47 (2005) 3336–3367, https://doi.org/10.1016/j.corsci.2005.05.053.
[2] I. Richardson, Guide to Nickel Aluminium Bronze for Engineers, (2016) 100. https://www.nickelinstitute.org/~/media/Files/MediaCenter/News/20160205-Guide_to_Nickel_Aluminium_Bronze_for_Engineers.ashx?la=en.
[3] H. Meigh, Cast and Wrought Aluminium Bronzes Properties, Processes and Structure, 1st ed., CRC Press, New York, 2000.
[4] Ministry of Defence, Defence Standard 02-747 Part 2 Requirements for Nickel Aluminium Bronze Castings and Ingots Part 2: Nickel Aluminium Bronze Naval Alloy Ingots and Sand Casting with Welding Permitted to the Wetted Surface, 2013.
[5] H. Li, D. Grudgings, N.P. Larkin, J. Norrish, M. Callaghan, L. Kuzmikova, Optimization of welding parameters for repairing NiAl bronze components, Mater. Sci. Forum 706–709 (2012) 706–709, https://doi.org/10.4028/www.scientific.net/MSF.706-709.2980.
[6] E.A. Culpan, A.G. Foley, The detection of selective phase corrosion in cast nickel aluminium bronze by acoustic emission techniques, J. Mater. Sci. 17 (1982) 953–964, https://doi.org/10.1007/BF00543513.
[7] H. Amegroud, A. Guenbour, A. Bellaouchou, Y.El aoufir, H. Lgaz, I.-M. Chung, A. A. Alrashdi, A comprehensive investigation of the electrochemical behavior of nickel-aluminum bronze alloy in alkaline solution: the effect of film formation

potential, Colloids Surf. A Physicochem. Eng. Asp. 614 (2021) 126126, https://doi.org/10.1016/j.colsurfa.2020.126126.
[8] Y. Ding, R. Zhao, Z. Qin, Z. Wu, L. Wang, L. Liu, W. Lu, Evolution of the Corrosion product film on nickel-aluminum bronze and its corrosion behavior in 3.5 wt% NaCl Solution, Mater. (Basel) 12 (2019) 209, https://doi.org/10.3390/ma12020209.
[9] S. Neodo, D. Carugo, J.A. Wharton, K.R. Stokes, Electrochemical behaviour of nickel–aluminium bronze in chloride media: influence of pH and benzotriazole, J. Electroanal. Chem. 695 (2013) 38–46, https://doi.org/10.1016/J.JELECHEM.2013.02.007.
[10] E. Skilbred, Corros. NAB Seawater (2016).
[11] G.S. Frankel, Pitting Corrosion of Metals: a Review of the Critical Factors, J. Electrochem. Soc. 145 (1998) 2186–2198, https://doi.org/10.1149/1.1838615.
[12] R.S. Oakley, J.C. Galsworthy, G.S. Fox, K.R. Stokes, Long-term and accelerated corrosion testing methods for cast nickel-aluminium bronzes in seawater, in: Corros. Behav. Prot. Copp. Alum. Alloy. Seawater, Elsevier Ltd, 2007: pp. 119–127. https://doi.org/10.1533/9781845693084.3.119.
[13] The American Petroleum Institute and The American Society of Mechanical Engineers, Fitness-For-Service API 579-1/ASME FFS-1, (2016) 1–1320.
[14] The Aluminium Bronze Advisory Service, Aluminium Bronze Alloys Corrosion Resistance Guide, (1981) Publication No: 80.
[15] S. Kou, Welding Metallurgy, 2003. https://doi.org/10.22486/iwj.v4i3.150243.
[16] S.S. Nayak, V.H. Baltazar Hernandez, Y. Okita, Y. Zhou, Microstructure–hardness relationship in the fusion zone of TRIP steel welds, Mater. Sci. Eng. A. 551 (2012) 73–81, https://doi.org/10.1016/J.MSEA.2012.04.096.
[17] S. Sriintharasut, B. Poopat, I. Phung-On, The effects of different types of welding current on the characteristics of nickel aluminum bronze using gas metal arc welding, Mater. Today Proc. 5 (2018) 9535–9542, https://doi.org/10.1016/j.matpr.2017.10.135.
[18] G. Van Boven, W. Chen, R. Rogge, The role of residual stress in neutral pH stress corrosion cracking of pipeline steels. Part I: pitting and cracking occurrence, Acta Mater. 55 (2007) 29–42, https://doi.org/10.1016/J.ACTAMAT.2006.08.037.
[19] H.A. Videla, L.K. Herrera, R.G. Edyvean, in: Corros, in: An updated overview of SRB induced corrosion and protection of carbon steel, 2005, NACE International, Houston, 2005, pp. 1–11.
[20] H.A. Videla, W.G. Characklis, Biofouling Microb. Influ. Corros. 29 (1992) 195–212.
[21] W.G. Characklis, Bioengineering report fouling Biofilm Development: a Process Analysis, Biotechnol. Bioeng. XXIII (1981) 1923–1960.
[22] P.Y. Qian, A. Cheng, R. Wang, R. Zhang, Marine biofilms: diversity, interactions and biofouling, Nat. Rev. Microbiol. 20 (2022) 671–684, https://doi.org/10.1038/s41579-022-00744-7.
[23] W.A. Hamilton, Biofilms: Microbial interactions and metabolic activities, in: M. Fletcher, T.R.G. Gray, J.G. Jones (Eds.), Ecol. Microb. Communities, Oxford University Press, 1987.
[24] I.B. Beech, J. Sunner, Biocorrosion: towards understanding interactions between biofilms and metals, Curr. Opin. Biotechnol. 15 (2004) 181–186, https://doi.org/10.1016/j.copbio.2004.05.001.
[25] T. Dobson, A. Yunnie, D. Kaloudis, N. Larossa, H. Coules, Biofouling and Corrosion Rate of Welded nickel aluminium bronze in natural and simulated seawater, Rev. Biofouling. (2024).
[26] Weldability, SIFMIG 44, n.d.
[27] ASTM International 2021 Stand. Pract. Prep. Substit. Ocean Water1998, D1141–D1198, 10.1520/D1141-98R08.2.
[28] ECHA, Sig Sulphide Test Data Sheet, (2016) EP017 110717. https://echamicrobiology.com/app/uploads/2016/06/EP90_Sig-Sulphide-Product-Data-Sheet_180717.pdf.
[29] ASTM, Standard Practice for Preparing, Cleaning, and Evaluating Corrosion Test Specimens, ASTM G1. i (1985) 505–510, https://doi.org/10.1520/G0001-03R17E01.2.
[30] Y. Zhao, Q. Guo, Z. Zhao, X. Wu, Y. Xing, Prediction of tensile strength degradation of corroded steel based on in-situ pitting evolution, Steel Compos. Struct. 46 (2023) 385–401, https://doi.org/10.12989/scs.2023.46.3.385.
[31] M. Cerit, K. Genel, S. Eksi, Numerical investigation on stress concentration of corrosion pit, Eng. Fail. Anal. 16 (2009) 2467–2472, https://doi.org/10.1016/J.ENGFAILANAL.2009.04.004.
[32] M. Hashim, F. Farhad, D. Smyth-Boyle, R. Akid, X. Zhang, P.J. Withers, Behavior of 316L stainless steel containing corrosion pits under cyclic loading, Mater. Corros. 70 (2019) 2009–2019, https://doi.org/10.1002/maco.201810744.
[33] Xinyi Zhang, Shuxin Li, Rui Liang, X. Zhang, S.. Li, R.. Liang, Effect of corrosion pits on fatigue life and crack initiation, in: ICF13, The Chinese Society of Theoretical and Applied Mechanics, Beijing, 2013.
[34] M.T.M.T. Hutchings, P.J. Withers, T.M. Holden, T. Lorentzen, Introduction to the characterization of residual stress by neutron diffraction, Taylor and Francis, Boca Raton, FL SE - 401 pages: illustrations; 25 cm, 2005. http://www.crcnetbase.com/isbn/9780203402818.
[35] B. Clausen, T. Lorentzen, T. Leffers, Self-consistent modelling of the plastic deformation of F.C.C. polycrstals and its implications for diffraction measurements of internal stresses, Acta Mater. 46 (1998) 3087–3098, https://doi.org/10.1016/S1359-6454(98)00014-7.
[36] R.C. Wimpory, C. Ohms, M. Hofmann, R. Schneider, A.G. Youtsos, Statistical analysis of residual stress determinations using neutron diffraction, Int. J. Press. Vessel. Pip. 86 (2009) 48–62, https://doi.org/10.1016/j.ijpvp.2008.11.003.
[37] J.A. Wharton, K.R. Stokes, The influence of nickel-aluminium bronze microstructure and crevice solution on the initiation of crevice corrosion, Electrochim. Acta 53 (2008) 2463–2473, https://doi.org/10.1016/j.electacta.2007.10.047.
[38] G.S. Frankel, N. Sridhar, Understanding localized corrosion, Mater. Today 11 (2008) 38–44, https://doi.org/10.1016/S1369-7021(08)70206-2.
[39] O.O. Fatoba, R. Leiva-Garcia, S.V. Lishchuk, N.O. Larrosa, R. Akid, Simulation of stress-assisted localised corrosion using a cellular automaton finite element approach, Corros. Sci. 137 (2018) 83–97, https://doi.org/10.1016/j.corsci.2018.03.029.
[40] Y. Lv, J. Guo, G. Zhang, L. Cao, X. Sun, Z. Qin, D.-H. Xia, Insights into the selective phase corrosion of as cast NiAl bronze alloy: effect of electrical properties of each phase's protective film, J. Alloy. Compd. 891 (2022) 162008, https://doi.org/10.1016/j.jallcom.2021.162008.
[41] A. Schüssler, H.E. Exner, The corrosion of nickel-aluminium bronzes in seawater-II. The corrosion mechanism in the presence of sulphide pollution, Corros. Sci. (1993), https://doi.org/10.1016/0010-938X(93)90018-C.
[42] Z. Qin, Q. Zhang, Q. Luo, Z. Wu, B. Shen, L. Liu, W. Hu, Microstructure design to improve the corrosion and cavitation corrosion resistance of a nickel-aluminum bronze, Corros. Sci. 139 (2018) 255–266, https://doi.org/10.1016/j.corsci.2018.04.043.
[43] B. Sabbaghzadeh, R. Parvizi, A. Davoodi, M.H. Moayed, Corrosion evaluation of multi-pass welded nickel-aluminum bronze alloy in 3.5% sodium chloride solution: a restorative application of gas tungsten arc welding process, Mater. Des. 58 (2014) 346–356, https://doi.org/10.1016/j.matdes.2014.02.019.
[44] H. Nady, N.H. Helal, M.M. El-Rabiee, W.A. Badawy, The role of Ni content on the stability of Cu-Al-Ni ternary alloy in neutral chloride solutions, Mater. Chem. Phys. 134 (2012) 945–950, https://doi.org/10.1016/j.matchemphys.2012.03.096.
[45] Y. Ding, Y. Lv, K. Chen, B. Zhao, Y. Han, L. Wang, W. Lu, Effects of microstructure on the stress corrosion cracking behavior of nickel-aluminum bronze alloy in 3.5% NaCl solution, Mater. Sci. Eng. A. 733 (2018), https://doi.org/10.1016/j.msea.2018.07.066.
[46] C. Dharmendra, K.P. Rice, B.S. Amirkhiz, M. Mohammadi, Atom probe tomography study of κ-phases in additively manufactured nickel aluminum bronze in as-built and heat-treated conditions, Mater. Des. 202 (2021) 109541, https://doi.org/10.1016/j.matdes.2021.109541.
[47] C. Dharmendra, A. Hadadzadeh, B.S. Amirkhiz, G.D. Janaki Ram, M. Mohammadi, Microstructural evolution and mechanical behavior of nickel aluminum bronze Cu-9Al-4Fe-4Ni-1Mn fabricated through wire-arc additive manufacturing, Addit. Manuf. 30 (2019) 100872, https://doi.org/10.1016/j.addma.2019.100872.
[48] T. Murray, S. Thomas, Y. Wu, W. Neil, C. Hutchinson, Selective laser melting of nickel aluminium bronze, Addit. Manuf. 33 (2020) 101122, https://doi.org/10.1016/j.addma.2020.101122.
[49] D. Nakhaie, A. Davoodi, A. Imani, The role of constituent phases on corrosion initiation of NiAl bronze in acidic media studied by SEM – EDS, AFM and SKPFM, Corros. Sci. 80 (2014) 104–110, https://doi.org/10.1016/j.corsci.2013.11.017.
[50] H.E. Coules, Contemporary approaches to reducing weld induced residual stress, Mater. Sci. Technol. 29 (2013) 4–18, https://doi.org/10.1179/1743284712Y.0000000106.
[51] R. Harriman, H. Anderson, J.D. Miller, The role of sea-salts in enhancing and mitigating surface water acidity, Water Air Soil Pollut. 85 (1995) 553–558, https://doi.org/10.1007/BF00476887.
[52] I.B. Beech, S.A. Campbell, Accelerated low water corrosion of carbon steel in the presence of a biofilm harbouring sulphate-reducing and sulphur-oxidising bacteria recovered from a marine sediment, Electrochim. Acta 54 (2008) 14–21, https://doi.org/10.1016/j.electacta.2008.05.084.
[53] W.G. Characklis, Biofilms and Corrosion: a Process Analysis Viewpoint, Int. Biodeteriation. 25 (1989) 323–326.
[54] S.G.Gomez de Saravia, M.F.L.L. de Mele, H.A. Videla, S.G.G. de Saravia, M.F.L.L. de Mele, H.A. Videla, An assessment of the early stages of microfouling and corrosion of 70:30 copper nickel alloy in the presence of two marine bacteria, Biofouling 1 (1989) 213–222, https://doi.org/10.1080/08927018909378109.
[55] T. Dobson, N. Larrosa, H. Coules, The role of corrosion pit topography on stress concentration, Eng. Fail. Anal. 157 (2024) 107900, https://doi.org/10.1016/j.engfailanal.2023.107900.
[56] R. Pennati, U. Rothbächer, Bioadhesion in ascidians: a developmental and functional genomics perspective, Interface Focus 5 (1) (2014) 10, https://doi.org/10.1098/rsfs.2014.0061.
[57] D.E. Barlow, K.J. Wahl, Optical Spectroscopy of Marine Bioadhesive Interfaces, Annu. Rev. Anal. Chem. 5 (2012) 229–251, https://doi.org/10.1146/annurev-anchem-061010-113844.
[58] N. Aldred, A.S. Clare, Mini-review: impact and dynamics of surface fouling by solitary and compound ascidians, Biofouling 30 (2014) 259–270, https://doi.org/10.1080/08927014.2013.866653.
[59] G.F. Kennell, R.W. Evitts, K.L. Heppner, A critical crevice solution and IR drop crevice corrosion model, Corros. Sci. 50 (2008) 1716–1725, https://doi.org/10.1016/j.corsci.2008.02.020.
[60] Z. Zhang, Z. Li, F. Wu, J. Xia, K. Huang, B. Zhang, J. Wu, A comparison study of crevice corrosion on typical stainless steels under biofouling and artificial configurations, Npj Mater. Degrad. 6 (2022), https://doi.org/10.1038/s41529-022-00301-w.
[61] R. Sangeetha, R. Kumar, M. Doble, R. Venkatesan, Barnacle cement: an etchant for stainless steel 316L? Colloids Surf. B Biointerfaces 79 (2010) 524–530, https://doi.org/10.1016/j.colsurfb.2010.05.009.
[62] United Nations, International Convention for the Safety of Life at Sea, 1974.
[63] M. Hazra, K.P. Balan, Failure of a nickel aluminium bronze (NAB) canned motor pump impeller working under polluted sea water – Influence of material selection, section thickness dependent microstructure and temper annealing heat treatment,

Eng. Fail. Anal. 70 (2016) 141–156, https://doi.org/10.1016/j.engfailanal.2016.07.010.
[64] Americal Bureau of Shipping, Guidance Notes on The Application of Ergonomics To Marine Systems, Houston, TX, 2018. https://ww2.eagle.org/content/dam/eagle/rules-and-guides/current/other/86_applicationsofergonomicstomarinesystems/ergo-gn_e-aug18.pdf.
[65] P. Vuong, A. McKinley, P. Kaur, Understanding biofouling and contaminant accretion on submerged marine structures, Npj Mater. Degrad. 7 (2023) 50, https://doi.org/10.1038/s41529-023-00370-5.

2024-03-23

Corrosion mechanisms of plasma welded Nickel aluminium bronze immersed in seawater

Dobson, Tamsin

Elsevier

Dobson T, Larrosa N, Reid M, et al., (2024) Corrosion Mechanisms of Plasma Welded Nickel Aluminium Bronze Immersed in Seawater. Corrosion Science, Volume 232, May 2024, Article number 112004

https://doi.org/10.1016/j.corsci.2024.112004